Transactions of Tianjin University (2022) 28:227–235
https://doi.org/10.1007/s12209-022-00334-x

RESEARCH ARTICLE

Modulating the Selectivity of Photocatalytic CO_2 Reduction in Barium Titanate by Introducing Oxygen Vacancies

Yi Wang[1,2] · Chengbo Zhang[1,2] · Rengui Li[1]

Received: 21 June 2022 / Revised: 19 July 2022 / Accepted: 21 August 2022 / Published online: 23 August 2022

Abstract
Artificial photosynthetic reduction of CO_2 into valuable chemicals is one of the most promising approaches to solve the energy crisis and decreasing atmospheric CO_2 emissions. However, the poor selectivity accompanied by the low activity of photocatalysts limits the development of photocatalytic CO_2 reduction. Herein, inspired by the use of oxygen vacancy engineering to promote the adsorption and activation of CO_2 molecules, we introduced oxygen vacancies in the representative barium titanate ($BaTiO_3$) photocatalyst for photocatalytic CO_2 reduction. We found that oxygen vacancies brought significant differences in the CO_2 photoreduction activity and selectivity of $BaTiO_3$. The intrinsic $BaTiO_3$ showed a low photocatalytic activity with the dominant product of CO, whereas $BaTiO_3$ with oxygen vacancies exhibited a tenfold improvement in photocatalytic activity, with a high selectivity of ~ 90% to CH_4. We propose that the presence of oxygen vacancies promotes CO_2 and H_2O adsorption onto the $BaTiO_3$ surface and also improves the separation and transfer of photogenerated carriers, thereby boosting the photocatalytic CO_2 reduction to CH_4. This work highlights the essential role of oxygen vacancies in tuning the selectivity of photocatalytic reduction of CO_2 into valuable chemicals.

Keywords Photocatalytic CO_2 reduction · Oxygen vacancy · Selectivity modulation · Barium titanate

Introduction

With the development of the economy and society, the massive combustion of fossil fuels has resulted in a rapid increase in CO_2 concentration in the atmosphere, leading to severe climate change [1–3]. The utilization of solar energy to achieve photocatalytic conversion of CO_2 into carbonaceous fuels is one of the most beneficial approaches to solve the above issue [4, 5]. However, CO_2 photoreduction with high performance and selectivity is challenging because the inert nature of CO_2 leads to difficult activation. Furthermore, the process from the activated intermediate to the reactant involves complex electron and proton transfer kinetically [6, 7]. Endeavors in photocatalytic CO_2 reduction since 1978 [8] involved the development of strategies including cocatalyst loading, surface modulation, and facet tailoring to modify the electronic and surface properties, such as light excitation [9], charge separation [10, 11], CO_2 adsorption and activation [12–15], surface reactive sites [16–18], and intermediates [19]. Although the diverse products of photocatalytic CO_2 reduction (including carbon monoxide [20], methane [21–24], methanol [25] or even multi-carbon products [26–28]) have been reported, strategies to precisely tune the selectivity of photocatalytic CO_2 reduction are still in their infancy.

Oxygen vacancies with relatively low formation energy on oxide surfaces have attacted many attentions [29, 30]. Oxygen vacancies were widely recognized to act as electron traps to promote the separation of photogenerated charges in photocatalysis [31–34]. In addition, the local electron enrichment caused by the appearance of oxygen vacancies changes the surface chemical environment of the photocatalyst and promotes the adsorption and activation of CO_2 in the photocatalytic CO_2 reduction reaction [35–39]. Previously, we realized selective CO_2 photoreduction to CO on the oxygen vacancy-involved hexagonal WO_3. Besides, the

Yi Wang and Chengbo Zhang have contributed equally to the work.

✉ Rengui Li
rgli@dicp.ac.cn

[1] State Key Laboratory of Catalysis, Dalian Institute of Chemical Physics, Chinese Academy of Sciences, Dalian National Laboratory for Clean Energy, Dalian 116023, China

[2] University of Chinese Academy of Sciences, Beijing 100049, China

in situ-generated oxygen vacancy lowers the CO_2 activation barrier and promotes the photocatalytic CO_2 reduction on WO_3 [40]. It was also reported that an oxygen vacancy has a pinning effect on the ferroelectric monodomain of the material after corona polarization, providing a continuous driving force for the separation and migration of photogenerated charge carriers [41]. However, the main function of oxygen vacancies in most studies is considered to improve the adsorption and activation of CO_2, with a lack of consideration of how oxygen vacancies affect the CO_2 reduction pathway to tune the selectivity of products.

Herein, taking barium titanate ($BaTiO_3$) as a prototype, we fabricated a series of $BaTiO_3$ with tunable concentrations of oxygen vacancies by $NaBH_4$ reduction for photocatalytic CO_2 reduction. The $BaTiO_3$ photocatalysts with oxygen vacancies showed a dramatic change in activity and selectivity of photocatalytic CO_2 reduction. Further investigations indicated that the oxygen vacancies not only changes the surface and electronic nature of the $BaTiO_3$, but also promotes the adsorption of CO_2 and H_2O molecules, which contribute to the controllable selectivity of the reduction of CO_2 from CO to CH_4. This work will be beneficial in fabricating the heterogeneous photocatalysts to tune the product distribution in photocatalytic CO_2 reduction into chemicals.

Experimental

Synthesis of Tetragonal $BaTiO_3$

$BaTiO_3$ was synthesized using a reported sol–gel method [42]. All the chemicals were analytically pure without purification. 0.01 mol barium acetate was dissolved in 3 mL of glacial acetic acid, heated to 353 K, and then 5 mL ethylene glycol methyl ether was added to form a particle-free viscous dispersion. 5.14 mL glacial acetic acid, 1.84 mL acetylacetone, 0.71 mL formamide, and 0.81 mL deionized (DI) water were added to the above dispersion and then vigorously stirred for 10 min (Marked as solution A). Solution B consisted of 0.01 mol of tetrabutyl titanate with 10 mL ethylene glycol methyl ether and 2 mL acetylacetone as the solvent. The solutions A and B were quickly mixed to form solution C. Solution C was stirred in the air for 5 h and then dried in an oven at 453 K for 24 h to form a red gel. The gel was ground and then further heated in a muffle oven to form $BaTiO_3$ nanocrystals.

$BaTiO_3$ with oxygen vacancies was synthesized by molten salt treatment with adding $NaBH_4$. 0.15 g of barium titanate, and 0.35 g of sodium borohydride were thoroughly grounded in a glove box, and then the mixture was heated in a tube furnace with a heating rate of 25 K/min to 598–698 K for 90 min in Ar flow of 200 mL/min. After the powder was cooled to room temperature, the sample was firstly washed with a stoichiometric amount of 3 mol/L hydrochloric acids and then washed with hot water to ensure that the boric acid was completely removed.

Characterization of the Catalyst

The morphology of the catalysts was characterized by scanning electron microscopy (Quanta 200 FEG, FEI) and high-resolution transmission electron microscopy (TECNAI G2 F30). The phase and crystallinity of the sample were determined via a Bruker D2 Phaser powder diffractometer using Cu Kα radiation ranging from 5° to 80°. The UV–visible diffuse reflectance experiment was carried out with a quartz cell using a UV–visible spectrophotometer (JASCO V-650). The EPR results were recorded by an electron paramagnetic resonance spectrometer (Bruker A200). A 325 nm-wavelength laser was selected as the Raman inlet light, and the experiments were performed using a Princeton Instruments Acton SpectraPro SP-2500 spectrometer.

Photocatalytic CO_2 Performance Measurement

Photocatalytic CO_2 reduction measurement was carried out in a homemade quartz reactor (Fig. S1). 50 mg catalyst was dispersed uniformly by ultrasonic agitation in 5 mL of saturated $KHCO_3$ solution. Afterward, high-purity CO_2 was purged into the reactor through the solution for 30 min. The reactor was kept gastight during the reaction. A 300 W Xe lamp was used as the light source. At regular intervals, the gas sample was withdrawn by syringe, and then analyzed by GC (Tianmei, 7900, 5A molecular sieve column with methane reformer and FID detector). For the isotope labeling experiments, the feed gas was replaced by $^{13}CO_2$, and the gas product was analyzed by GC–MS.

Electrochemical Measurement

Electrodes were prepared by the drop coating method, with 5 mg catalyst dispersed into 5 mL of Nafion ethanol solution (0.25 wt%). After vigorous stirring, 1 mL of solution was added dropwise onto a 2×1 cm FTO substrate, and then the electrode was dried at 453 K. A saturated calomel electrode and 0.5 mol/L sodium sulfite solution were chosen as the reference electrode and the electrolyte, respectively.

In Situ FTIR Experiments

In situ FTIR experiments were carried out on a Nicolet 380 spectrometer with a TRS-20 MHz detector. A homemade quartz cell was utilized for placing the sample wafer. Before FTIR experiment, the catalyst was pre-heated at 393 K for 2 h. Ar, CO_2, and CO_2 purged through water were introduced into the cell sequentially. The signal was collected when it

became stable. The sample was then irradiated by a 300 W Xe lamp after the sample reached a steady state in water vapor and CO_2 atmosphere. The signal was collected once light irradiation was introduced into the cell.

Results and Discussion

$BaTiO_3$ is a typical ferroelectric semiconductor used in photocatalysis. Despite reports that introducing oxygen vacancies in perovskite $BaTiO_3$ could promote photocatalytic N_2 reduction to NH_3 [42], few studies have focused on the effect of oxygen vacancies in $BaTiO_3$ for CO_2 reduction. The $BaTiO_3$ crystal consists an ABO_3 unit cell (Fig. 1a), in which the oxygen atom can be removed by chemical reduction [43], resulting in the creation of an oxygen vacancy on the surface, making it possible to tune the oxygen vacancy gradient. Tetragonal $BaTiO_3$ nanocrystals was synthesized as previously reported [42]. X-ray diffraction patterns of the as-prepared $BaTiO_3$ are shown in Fig. 1b. All the diffraction peaks can be indexed to tetragonal $BaTiO_3$ (JCPSB No.05-0626). Note that there is no significant peak splitting at $2\theta = 45°$, indicating that no cubic or mixture structure was present. TEM images show relatively regular nanocrystal features with a particle size of 50–100 nm (Fig. 1c). High-resolution TEM image in Fig. 1d shows that the length of the lattice spacing is 4.04 Å, ascribed to the typical (001) plane of the tetragonal $BaTiO_3$, which is consistent with the XRD patterns.

$BaTiO_3$ with oxygen vacancies gradient was obtained by molten salt treatment with adding $NaBH_4$ under different temperatures. The XRD patterns in Fig. 2a show that the intensity of the main diffraction peak displays no obvious change when the temperature was below 673 K, whereas $BaTiO_3$ treated at 698 K displayed a wider full width at half maximum (FWHM) and weaker peak intensity, demonstrating a slight decrease in crystallinity. No additional diffraction peak appears, even when the temperature is higher than the Curie temperature. The morphology of $BaTiO_3$ can be maintained after the treatment under different temperatures (Fig. S2). UV–visible diffusion reflection spectroscopy was then carried out to study the absorbance difference. As shown in Fig. 2b, as the temperature increases, the absorption of the $BaTiO_3$ in the visible light region gradually

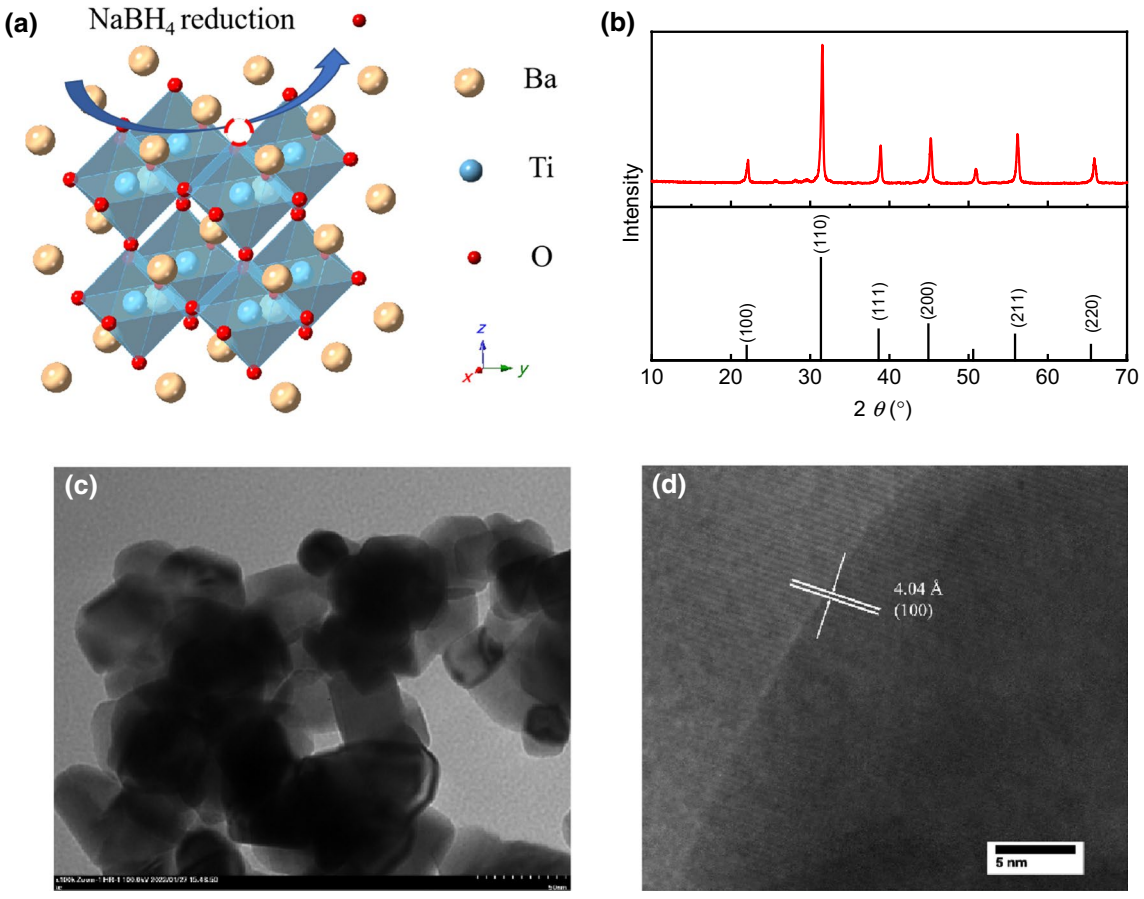

Fig. 1the author modified the figures in this paper for a more standardized expression, please replace with the figures in the attachment uploaded Schematic structure and characterization of as-prepared $BaTiO_3$. **a** Illustration of the tetragonal $BaTiO_3$ crystal structure; **b** XRD pattern of as-prepared $BaTiO_3$; **c** TEM image of tetragonal $BaTiO_3$; **d** High-resolution TEM image of tetragonal $BaTiO_3$

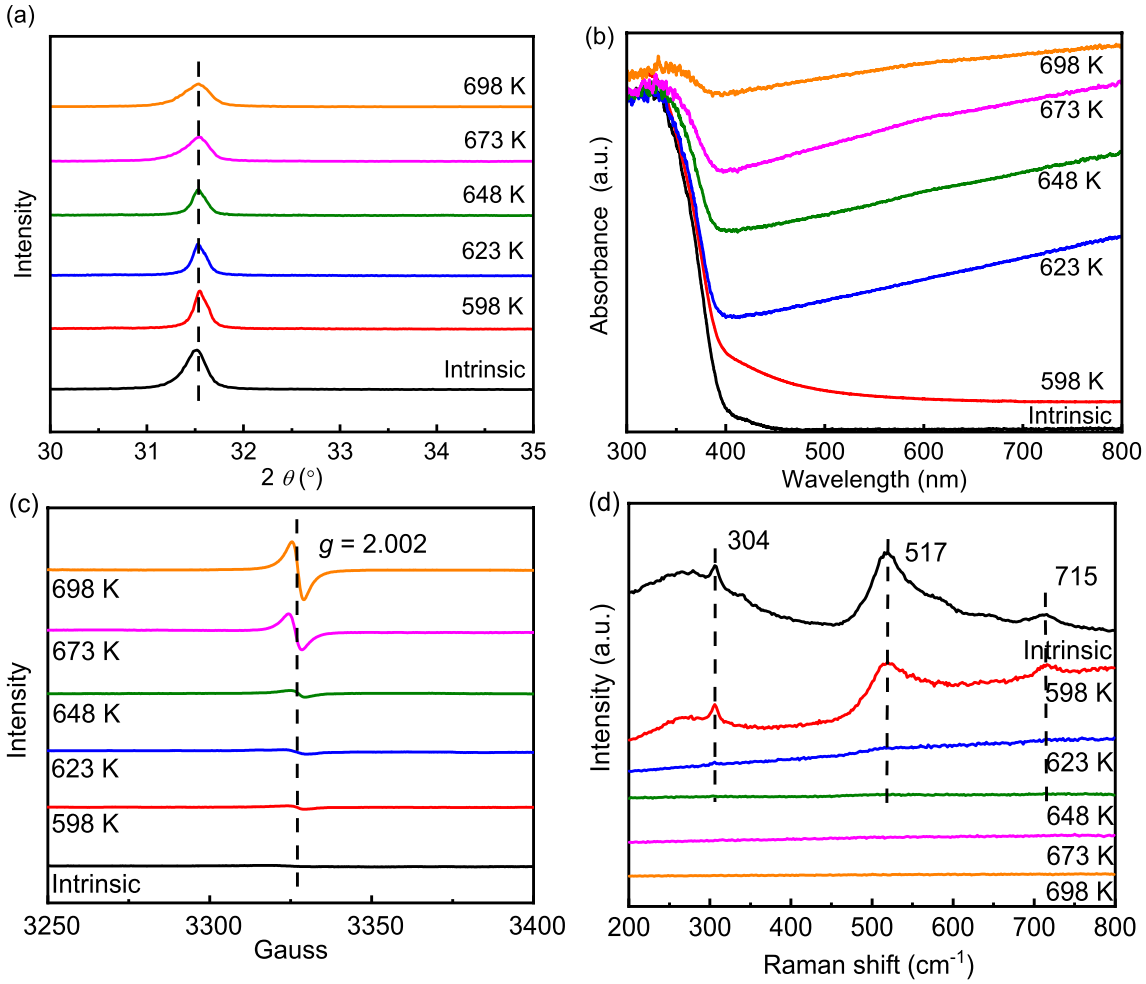

Fig. 2 Characterization of intrinsic and oxygen vacancy-involved $BaTiO_3$. **a** Enlarged XRD pattern, **b** UV–visible spectra, **c** EPR spectra, and **d** Raman spectra of intrinsic and oxygen vacancy-involved $BaTiO_3$. The temperatures marked in the figures refer to the sample with the corresponding reduction temperature

increases. It is generally accepted that the increased absorption intensity in the visible light region can be ascribed as the increase in low-valent metal species, which confirms the gradual increase of oxygen vacancies in the $BiTiO_3$. It has been demonstrated that the loss of oxygen in the lattice would induce the slight decrease in cell volume and cell parameters [37]. The presence of oxygen vacancies was also verified by the electron paramagnetic resonance (EPR) spectra, as shown in Fig. 2c. An obvious signal appeared at $g = 2.002$, corresponding to the signal of free electrons captured by holes, was observed, and the intensity increased gradually with the increase in the reduction temperature. The intensity of the signal displays a consistent trend versus the reduction temperature, illustrating that the concentration of oxygen vacancies increases with the reduction temperature. Analysis of Raman spectra was carried out to verify the structure evolution of $BiTiO_3$ (Fig. 2d). A typical tetragonal phase of $BaTiO_3$ for the intrinsic $BiTiO_3$ exhibits the characteristic sharp peak at 270 cm^{-1} and broad bands at 517 cm^{-1} and 705 cm^{-1} [44]. Note that when the $BaTiO_3$ was reduction treated at 598 K, the corresponding Raman peak intensity decreases, and the FWHM increases. Further increasing the reduction temperature to 623 K, the characteristic peak corresponding to the $BaTiO_3$ disappears, which may be due to the destruction of the surface structure by the removal of oxygen and forming an amorphous layer, which is consistent with the previously reported results [37, 45, 46]. The above results demonstrate that the $BaTiO_3$ with different oxygen vacancy concentrations can be obtained by molten salt treatment in the presence of $NaBH_4$ at different temperatures.

Photocatalytic CO_2 reduction performance was examined in the CO_2 gas saturated $KHCO_3$ solution. As shown in Fig. 3a, b, both intrinsic and oxygen-vacancy-involved $BaTiO_3$ samples enable the realization of the photocatalytic CO_2 reaction but exhibit a significant

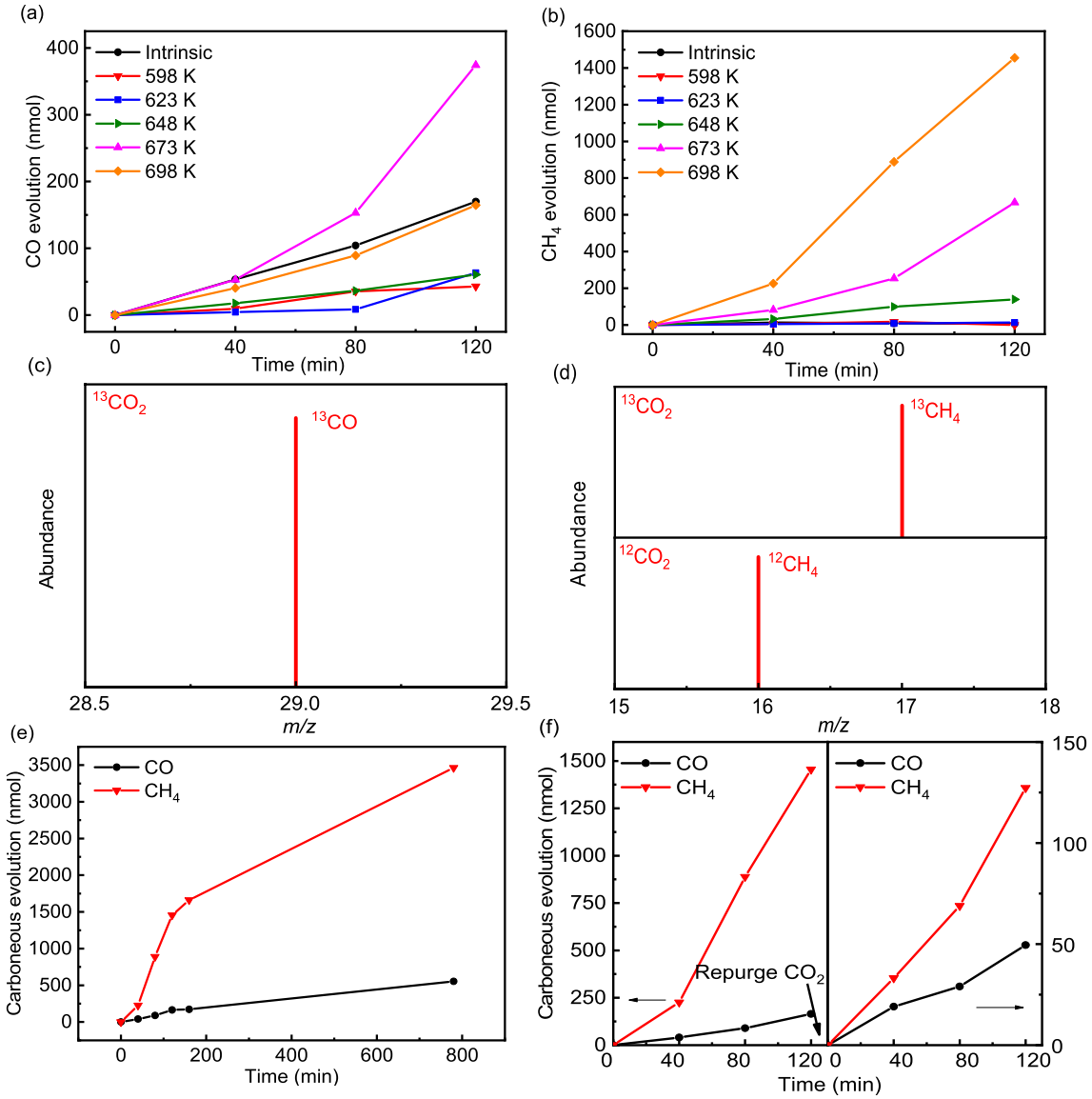

Fig. 3 Photocatalytic performance of the intrinsic and oxygen vacancy-involved $BaTiO_3$. Time course of **a** CO and **b** CH_4 evolution for intrinsic and oxygen vacancy-involved $BaTiO_3$ under UV–visible illumination in saturated CO_2-$KHCO_3$ solution. Mass spectra extracted from GC–MS analysis of the products **c** CO and **d** CH_4 with isotope labeling using $^{13}CO_2$. **e** Long-time course reaction performance for $BaTiO_3$ reduced at 698 K. **f** CO and CH_4 evolution comparison for $BaTiO_3$ reduced at 698 K and that re-reduced at 698 K. The temperatures marked in the figures refer to the sample with the corresponding reduction temperature

difference in photocatalytic activity and selectivity. For intrinsic $BaTiO_3$, the only product was CO with no CH_4 was detected. With the increase in the reducing temperature to create oxygen vacancies in the $BaTiO_3$, the amount of CO was reduced, whereas CH_4 was detected in the product and the CH_4 amount gradually increased. Blank experiments, including without introduction of $BaTiO_3$ or without light irradiation, were also performed to confirm the produced CO and CH_4 were indeed originated from the photocatalytic CO_2 reduction on $BaTiO_3$ (Fig. S4). The CH_4 selectivity of $BaTiO_3$ reduced at 698 K in 2 h was measured to be ~ 90%. A direct comparison of real-time gas chromatograms was also shown in Fig. S5. When the reduction temperature exceeds 698 K, the obtained sample is a flammable solid with a black metallic luster. The $BiTiO_3$ catalyst reduced at 673 K exhibited a better photocatalytic activity of CO_2 reduction to CO, whereas the $BaTiO_3$ reduced at 698 K was optimized to be superior to others toward CH_4 and overall carbonaceous products (Fig. S6). Photocatalytic CO_2 reduction of $BaTiO_3$ reduced at 698 K in pure water were also conducted (Fig. S7). Given the low solubility of CO_2 in water, the activity in water

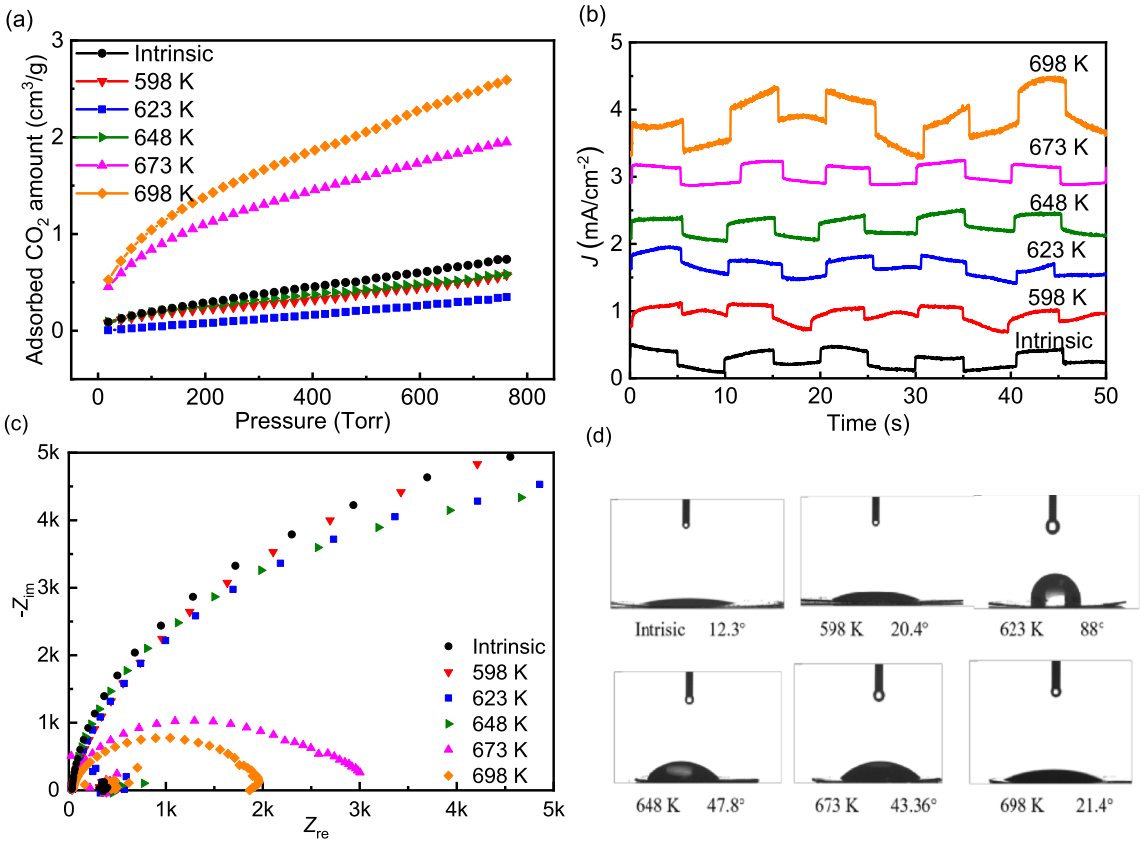

Fig. 4 Electronic and surface characterization of intrinsic and oxygen vacancy-involved $BaTiO_3$. **a** CO_2 adsorption spectra of intrinsic and oxygen vacancy-involved $BaTiO_3$. **b** Photocurrent density of intrinsic and oxygen vacancy-involved $BaTiO_3$ under light irradiation. **c** EIS spectra of intrinsic and oxygen vacancy-involved $BaTiO_3$. **d** Contact angle of the intrinsic and oxygen vacanvy-involved $BaTiO_3$. The temperatures marked in the figures refer to the sample with the corresponding reduction temperature

was found to be far below that in $KHCO_3$-CO_2 saturated solution.

Isotope labeling experiments with $^{13}CO_2$ as the reactant were carried out to determine the source of the product. As shown in Fig. 3c, d, when the reactant is $^{12}CO_2$, only a single peak appears at the position of $m/z = 28$, which corresponds to the reduction product of CO from $^{12}CO_2$. When the reactant was replaced by $^{13}CO_2$, a new peak appeared at the position of $m/z = 29$, which proved that CO is the product of CO_2 reduction. Moreover, when the reactant changed from $^{12}CO_2$ to $^{13}CO_2$, the peak position in the GC–MS spectrum changed from $m/z = 16$ to 17, which verified that the product of CH_4 comes from CO_2 photoreduction rather than possible contaminants. To determine the stability of the $BaTiO_3$ catalyst, as shown in Fig. 3e, f, the time curve and cycling reaction of the $BaTiO_3$ catalyst were conducted. The photocatalytic activity of the $BaTiO_3$ catalyst gradually decreases after long-term reaction. When the $BaTiO_3$ was retreated by $NaBH_4$ reduction, the photocatalytic performance of the catalyst significantly decreases, which may be due to the over-reduction of the catalyst, leading to the collapse of the surface structure. Although the long-term stability of the $BaTiO_3$ still requires improvement, the selectivity of CO_2 photoreduction toward CH_4 was maintained after cycling reactions for a long period.

To examine the presence of oxygen vacancies on the selectivity in photocatalytic CO_2 reduction, CO_2 adsorption and electrochemical measurements were carried out. As shown in Figs. 4a and S8, when the reduction temperature was tuned between 598 and 648 K, the CO_2 adsorption capacity abnormally decreased, which may be caused by the formation of a metastable structure that destroyed the original CO_2 adsorption sites. When the reduction temperature reaches 673 K, the CO_2 adsorption capacity dramatically increases. Note that the CO_2 adsorption changes is consistent with the trend of CO_2 photoreduction performance, indicating that the oxygen vacancies may change the surface nature of $BaTiO_3$, subsequently influencing the CO_2 adsorption and activation and causing the differences in CO_2 photoreduction. Furthermore, it is recognized that the CO_2 photoreduction toward CH_4 involves eight electrons and eight protons transfer process [47], for which photogenerated carrier transport also plays a critical role in the whole reaction process. As shown in Fig. 4b, the $BaTiO_3$ reduced at 698 K

with oxygen vacancies exhibits an enhanced photoelectric response compared to intrinsic $BaTiO_3$. In addition, the electrochemical impedance spectrum (EIS) measurements demonstrate that the $BaTiO_3$ reduced at 698 K possesses the smallest arc radius on resistance, indicating a better interfacial electron transfer on the $BaTiO_3$ with oxygen vacancies.

The selectivity of CO_2 reduction is not only correlated with the CO_2 adsorption and electron migration, but also related to the adsorption capacity of H_2O molecules. We further measured the contact angle for water molecules on the intrinsic and oxygen vacancy-involved $BaTiO_3$. As shown in Fig. 4d, the contact angle to water molecules of $BaTiO_3$ displays a trend of increasing first and then declining, and the $BaTiO_3$ with the reduction temperature of 623 K exhibits the largest contact angle to the water molecules. As the reduction temperature gradually increased, the $BiTiO_3$ surface became hydrophilic gradually, accompanied by the gradual generation of CH_4. The results indicates that it is essential for the $BiTiO_3$ photocatalyst to adsorb water molecules for subsequent proton-coupled electron transfer to produce CH_4.

To further elucidate the photocatalytic CO_2 reduction mechanism, in situ Fourier transform infrared spectrum (FTIR) measurements were performed. For intrinsic $BaTiO_3$, as shown in Fig. 5a, a new peak attributed to HCO_3^- appeared at 1760 cm^{-1}. When CO_2 and water vapor were introduced into the reactor, following irradiation, the intensity of the peak at 1640 cm^{-1} ascribed to OH^- dramatically increased, indicating strong adsorption of water molecules. The peak at 1760 cm^{-1} vanished, and a new peak attributed to CO emerged, demonstrating that the CO_2 photoreduction occurs on the intrinsic $BaTiO_3$ with an ordinary process from $CO_2 \rightarrow HCO_3^- \rightarrow CO$, as we previously reported [34]. To further elaborate on the reaction pathway, FTIR experiment was carried out on the oxygen vacancy-involved $BiTiO_3$ under the same condition. It was found that a weak peak corresponding to the CH_3O^- was formed around 1160 cm^{-1}, which was considered to be an intermediate in the "Carbene Pathway" [48].

It is widely recognized that CO_2 photoreduction to CH_4 involves a process of CO_2 adsorption to charge transfer and subsequent reaction with adsorbed CO_2. Therefore, based on the results above, CO_2 and water adsorption directly determine the amount of reactants, which further determines the overall reduction of CO_2 to carbonaceous products. Furthermore, the selectivity of CO_2 toward CH_4 is directly related to the electron concentration on the surface. As shown in Scheme 1, by rational design and treatment of the $BaTiO_3$ catalyst, oxygen vacancies with a proper concentration would not only facilitate CO_2 adsorption and activation but also provide sufficient photogenerated carriers to the surface for water oxidation and subsequent proton coupling electron transfer to produce CH_4.

Conclusion

In summary, we obtained $BaTiO_3$ with different oxygen vacancy concentrations using the molten salt treatment in the presence of $NaBH_4$ and found that the presence of oxygen vacancies significantly affects the activity and selectivity of photocatalytic CO_2 reduction. Intrinsic $BaTiO_3$ shows a low photocatalytic activity with the dominant product of CO, whereas $BaTiO_3$ with oxygen vacancies exhibited a tenfold improvement in photocatalytic activity with a high selectivity of ~ 90% toward CH_4. We proposed that the presence of oxygen vacancies benefits CO_2 and H_2O adsorption onto the $BaTiO_3$ surface and also improves the separation and transfer of photogenerated carriers, thereby boosting the selective photocatalytic CO_2 reduction to methane. A proper oxygen vacancy concentration would optimize the surface chemical and electronic structure to further control the surface reactant concentration, leading to a relatively

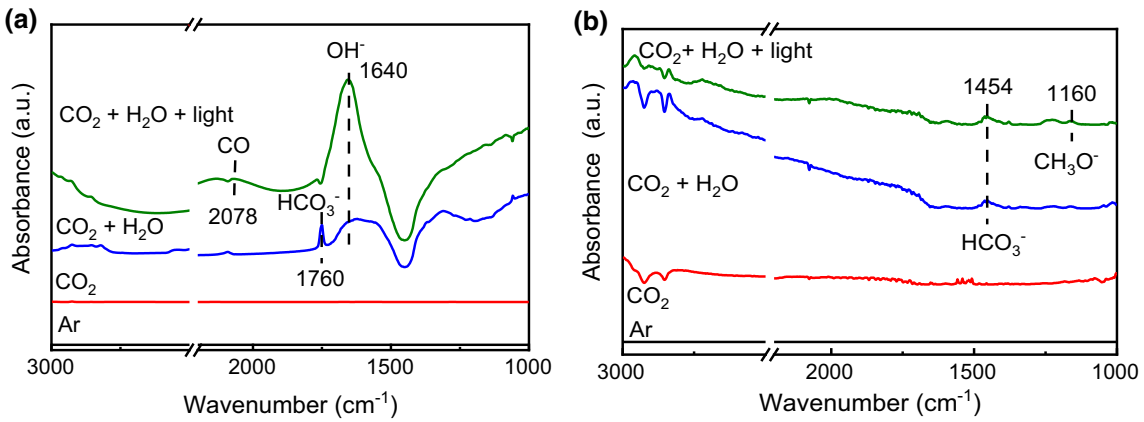

Fig. 5 In situ FTIR spectra of intrinsic and oxygen vacancy-involved $BaTiO_3$: **a** $BaTiO_3$ and **b** $BaTiO_3$ with oxygen vacancies

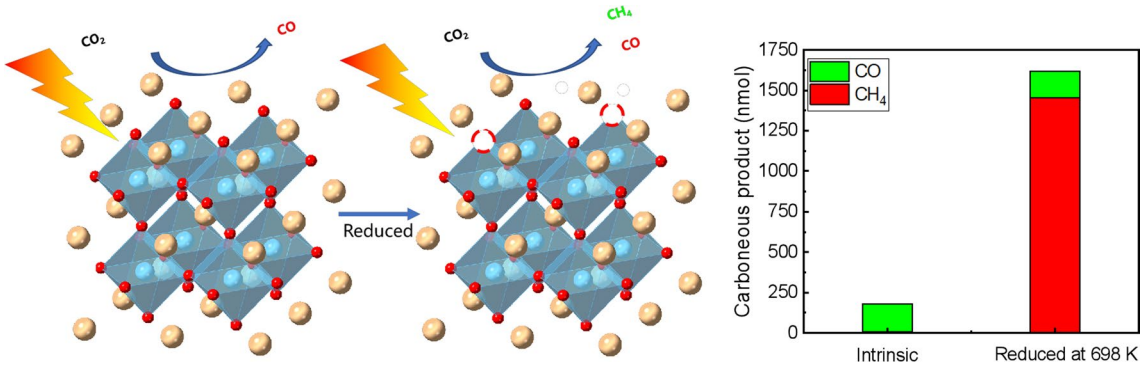

Scheme 1 Schematic illustration of CO_2 photoreduction on intrinsic and oxygen vacancy-involved $BaTiO_3$

high concentration and selectivity. Our work highlights the essential role of oxygen vacancies in tuning the selectivity of photocatalytic CO_2 reduction into valuable chemicals.

Supplementary Information The online version contains supplementary material available at https://doi.org/10.1007/s12209-022-00334-x.

Acknowledgements The work was supported by the National Key Research and Development Program of China (2021YFA1502300), National Natural Science Foundation of China (Nos. 22090033), Youth Innovation Promotion Association of the Chinese Academy of Sciences and the National Youth Talent Support Program.

Declarations

Conflict of interest The authors declare that there is no conflict of interest.

References

1. Navarro-Jaén S, Virginie M, Bonin J et al (2021) Highlights and challenges in the selective reduction of carbon dioxide to methanol. Nat Rev Chem 5(8):564–579
2. Fu JW, Jiang KX, Qiu XQ et al (2020) Product selectivity of photocatalytic CO_2 reduction reactions. Mater Today 32:222–243
3. Nahar S, Zain MFM, Kadhum AAH et al (2017) Advances in photocatalytic CO_2 reduction with water: a review. Materials 10(6):629
4. Zhang GG, Li GS, Heil T et al (2019) Tailoring the grain boundary chemistry of polymeric carbon nitride for enhanced solar hydrogen production and CO_2 reduction. Angew Chem Int Ed Engl 58(11):3433–3437
5. Ran J, Jaroniec M, Qiao SZ (2018) Cocatalysts in semiconductor-based photocatalytic CO_2 reduction: achievements, challenges, and opportunities. Adv Mater 30(7):1704649
6. Chang XX, Wang T, Gong JL (2016) CO_2 photo-reduction: insights into CO_2 activation and reaction on surfaces of photocatalysts. Energy Environ Sci 9(7):2177–2196
7. Wagner A, Sahm CD, Reisner E (2020) Towards molecular understanding of local chemical environment effects in electro- and photocatalytic CO_2 reduction. Nat Catal 3(10):775–786
8. Halmann M (1978) Photoelectrochemical reduction of aqueous carbon dioxide on p-type gallium phosphide in liquid junction solar cells. Nature 275(5676):115–116
9. Chen XB, Liu L, Yu PY et al (2011) Increasing solar absorption for photocatalysis with black hydrogenated titanium dioxide nanocrystals. Science 331(6018):746–750
10. Chen F, Ma TY, Zhang TR et al (2021) Atomic-level charge separation strategies in semiconductor-based photocatalysts. Adv Mater 33(10):2005256
11. Dong CC, Ji JH, Yang Z et al (2019) Research progress of photocatalysis based on highly dispersed titanium in mesoporous SiO_2. Chin Chem Lett 30(4):853–862
12. Huo HL, Liu D, Feng H et al (2020) Double-shelled Cu_2O/MnO_x mesoporous hollow structure for CO_2 photoreduction with enhanced stability and activity. Nanoscale 12(26):13912–13917
13. Qiu CH, Bai S, Cao WJ et al (2020) Tunable syngas synthesis from photocatalytic CO_2 reduction under visible-light irradiation by interfacial engineering. Trans Tianjin Univ 26(5):352–361
14. Zhao ZJ, Liu ZL, Zhu ZX et al (2021) Ultrathin zinc selenide nanosheet-based intercalation hybrid coupled with CdSe quantum dots showing enhanced photocatalytic CO_2 reduction. Chin Chem Lett 32(8):2474–2478
15. Yoshino S, Takayama T, Yamaguchi Y et al (2022) CO_2 reduction using water as an electron donor over heterogeneous photocatalysts aiming at artificial photosynthesis. Acc Chem Res 55(7):966–977
16. Collado L, Reñones P, Fermoso J et al (2022) The role of the surface acidic/basic centers and redox sites on TiO_2 in the photocatalytic CO_2 reduction. Appl Catal B Environ 303:120931
17. Lan ZA, Wang XC (2015) ChemInform abstract: merging surface organometallic chemistry with graphitic carbon nitride photocatalysis for CO_2 photofixation. ChemCatChem 7(9):1422–1423
18. Ye LQ, Wu D, Chu KH et al (2016) Phosphorylation of g-C_3N_4 for enhanced photocatalytic CO_2 reduction. Chem Eng J 304:376–383

19. Liu Q, Cheng H, Chen TX et al (2022) Regulating the *OCCHO intermediate pathway towards highly selective photocatalytic CO_2 reduction to CH_3CHO over locally crystallized carbon nitride. Energy Environ Sci 15(1):225–233
20. Xi GC, Ouyang SX, Li P et al (2012) Ultrathin $W_{18}O_{49}$ nanowires with diameters below 1 nm: synthesis, near-infrared absorption, photoluminescence, and photochemical reduction of carbon dioxide. Angew Chem Int Ed Engl 51(10):2395–2399
21. Tahir M, Amin NS (2015) Indium-doped TiO_2 nanoparticles for photocatalytic CO_2 reduction with H_2O vapors to CH_4. Appl Catal B Environ 162:98–109
22. Dimitrijevic NM, Vijayan BK, Poluektov OG et al (2011) Role of water and carbonates in photocatalytic transformation of CO_2 to CH_4 on titania. J Am Chem Soc 133(11):3964–3971
23. Wang Y, Zhang ZZ, Zhang LN et al (2018) Visible-light driven overall conversion of CO_2 and H_2O to CH_4 and O_2 on 3D-SiC@2D-MoS_2 heterostructure. J Am Chem Soc 140(44):14595–14598
24. Li XD, Sun YF, Xu JQ et al (2019) Selective visible-light-driven photocatalytic CO_2 reduction to CH_4 mediated by atomically thin $CuIn_5S_8$ layers. Nat Energy 4(8):690–699
25. Zeng GT, Qiu J, Li Z et al (2014) CO_2 reduction to methanol on TiO_2-passivated GaP photocatalysts. ACS Catal 4(10):3512–3516
26. Dai WL, Xu H, Yu JJ et al (2015) Photocatalytic reduction of CO_2 into methanol and ethanol over conducting polymers modified Bi_2WO_6 microspheres under visible light. Appl Surf Sci 356:173–180
27. Liu YY, Huang BB, Dai Y et al (2009) Selective ethanol formation from photocatalytic reduction of carbon dioxide in water with $BiVO_4$ photocatalyst. Catal Commun 11(3):210–213
28. Sun SM, Watanabe M, Wu J et al (2018) Ultrathin $WO_3{\cdot}0.33H_2O$ nanotubes for CO_2 photoreduction to acetate with high selectivity. J Am Chem Soc 140(20):6474–6482
29. Li H, Li J, Ai ZH et al (2018) Oxygen vacancy-mediated photocatalysis of BiOCl: reactivity, selectivity, and perspectives. Angew Chem Int Ed Engl 57(1):122–138
30. Wang JL, Kang SH, Zhu XG et al (2021) Highly ordered Nb_2O_5 nanochannel film with rich oxygen vacancies for electrocatalytic N_2 reduction: inactivation and regeneration of electrode. Chin Chem Lett 32(9):2833–2836
31. Yang S, Halliburton LE, Manivannan A et al (2009) Photoinduced electron paramagnetic resonance study of electron traps in TiO_2 crystals: oxygen vacancies and Ti^{3+} ions. Appl Phys Lett 94(16):162114
32. Lei FC, Sun YF, Liu KT et al (2014) Oxygen vacancies confined in ultrathin indium oxide porous sheets for promoted visible-light water splitting. J Am Chem Soc 136(19):6826–6829
33. Liao JZ, Li KL, Ma H et al (2020) Oxygen vacancies on the BiOCl surface promoted photocatalytic complete NO oxidation via superoxide radicals. Chin Chem Lett 31(10):2737–2741
34. Ma ZY, Li PH, Ye LQ et al (2017) Oxygen vacancies induced exciton dissociation of flexible BiOCl nanosheets for effective photocatalytic CO_2 conversion. J Mater Chem A 5(47):24995–25004
35. Wu SQ, Wang JB, Li QC et al (2021) Bi/BiOCl nanosheets enriched with oxygen vacancies to enhance photocatalytic CO_2 reduction. Trans Tianjin Univ 27(2):155–164
36. Li Q, Liu YN, Wan Z et al (2022) Microwave-assisted synthesis of oxygen vacancy associated TiO_2 for efficient photocatalytic nitrate reduction. Chin Chem Lett 33(8):3835–3841
37. Jiang LS, Li Y, Wu XY et al (2021) Rich oxygen vacancies mediated bismuth oxysulfide crystals towards photocatalytic CO_2-to-CH_4 conversion. Sci China Mater 64(9):2230–2241
38. Ji YF, Luo Y (2016) New mechanism for photocatalytic reduction of CO_2 on the anatase TiO_2 (101) surface: the essential role of oxygen vacancy. J Am Chem Soc 138(49):15896–15902
39. Ye LQ, Deng Y, Wang L et al (2019) Bismuth-based photocatalysts for solar photocatalytic carbon dioxide conversion. ChemSusChem 12(16):3671–3701
40. Wang Y, Liu RZ, Shi M et al (2022) Photo-induced carbon dioxide reduction on hexagonal tungsten oxide via an oxygen vacancies-involved process. Chin Chem Lett. https://doi.org/10.1016/j.cclet.2022.02.006
41. Yu HJ, Chen F, Li XW et al (2021) Synergy of ferroelectric polarization and oxygen vacancy to promote CO_2 photoreduction. Nat Commun 12(1):1–10
42. Zhao Z, Wang DD, Gao R et al (2021) Magnetic-field-stimulated efficient photocatalytic N_2 fixation over defective $BaTiO_3$ perovskites. Angew Chem Int Ed Engl 60(21):11910–11918
43. Zhao ZY, Li GR, Wang Z et al (2019) Black $BaTiO_3$ as multifunctional sulfur immobilizer for superior lithium sulfur batteries. J Power Sources 434:226729
44. Hayashi H, Nakamura T, Ebina T (2013) In-situ Raman spectroscopy of $BaTiO_3$ particles for tetragonal-cubic transformation. J Phys Chem Solids 74(7):957–962
45. Guo M, Lu JQ, Wu YN et al (2011) UV and visible Raman studies of oxygen vacancies in rare-earth-doped ceria. Langmuir 27(7):3872–3877
46. Wang YT, Cai JM, Wu MQ et al (2018) Rational construction of oxygen vacancies onto tungsten trioxide to improve visible light photocatalytic water oxidation reaction. Appl Catal B Environ 239:398–407
47. Kovacic Z, Likozar B, Hus M (2020) Photocatalytic CO_2 reduction: a review of ab initio mechanism, kinetics, and multiscale modeling simulations. ACS Catal 10(24):14984–15007
48. Tan SS, Zou LD, Hu E (2008) Kinetic modelling for photosynthesis of hydrogen and methane through catalytic reduction of carbon dioxide with water vapour. Catal Today 131(1–4):125–129

Dr. Rengui Li received his Ph.D. degree from Dalian Institute of Chemical Physics (DICP), Chinese Academy of Sciences in 2014. He worked as a visiting research associate in Prof. K. Domen's group at the University of Tokyo and Prof. Harry Atwater's group at California Institute of Technology. He was promoted as a full professor at DICP at 2018. His research interest is focused on the photocatalytic solar energy conversion. He has published more than 70 papers on Joule, Nature Commun., Angew. Chem. Int. Ed., Adv. Mater. etc., with more than 5500 citations. Dr. Rengui Li won various awards including Young Scientist Prize at International Congress on Catalysis and Rising Star in Catalysis of China. At present, he serves as the editorial board member of "Chinese Journal of Catalysis," "Chinese Chemical Letters" and "Journal of Applied Chemistry."